

RESEARCH ARTICLE

A Sensitivity Study of Butler Matrices: Application to an SIW Extended Beam Matrix at 28 GHz

GIUSEPPE ACRI¹, JORDAN CORSI², FLORENCE PODEVIN², (Member, IEEE),
EMMANUEL PISTONO², PHILIPPE FERRARI², (Senior Member, IEEE),
AND LUIGI BOCCIA³, (Senior Member, IEEE)

¹Nxp Semiconductors, 31100 Toulouse, France

²RFIC-Laboratory, University of Grenoble Alpes, 38400 Grenoble, France

³MAIC-Laboratory, University of Calabria, 87036 Rende, Italy

Corresponding author: Luigi Boccia (luigi.boccia@unical.it)


ABSTRACT In this paper, a detailed sensitivity study of Butler matrices is proposed. In particular, a Monte Carlo analysis is carried out on each block constituting the matrix to estimate its impact on the overall performance. The isolation level of the crossover transmission path is hence proved to be a critical part of the Butler matrix design. As it will be shown using both full-wave analysis and analytical equations, an isolation of 30 dB should be reached in order to guarantee proper operation of the matrix. These outcomes were experimentally proved by designing two 28 GHz Substrate Integrated Waveguide (SIW) 4×4 Butler matrices as a demonstrator in the framework of the extended beam concept. Thanks to the crossover transmission path high isolation, the measured results show an insertion loss of 2.13 ± 0.7 dB and a maximum output progressive phase deviation of -15.5° and $+16.9^\circ$. Based on $0.5 \lambda_0$ evenly spaced isotropic antennas, those results enable a spatial coverage from -89.4° to 83.1° with a maximum loss of 2.2 dB and a ripple of 1.1 dB for the array factor as compared to the $-48.6^\circ/+48.6^\circ$ spatial coverage, 3.7-dB of ripple of the conventional 4×4 Butler matrix array.

INDEX TERMS Butler matrix, beam forming network, extended beam, sensitivity study, millimeter-wave.

I. INTRODUCTION

Networking technologies have become increasingly omnipresent over the past two decades. In particular, 5G and future 6G and beyond are expected to support significantly faster mobile broadband speeds, lower latencies and hundreds of times more capacity than the current 4G while also enabling the full potential of the Internet of Things [1]. Specifically, the underemployed spectrum in the millimeter-wave (mm-wave) frequency bands (30-300 GHz) might be seen as a potentially profitable solution for achieving the aforementioned goals. Unfortunately, at mm-waves, the electromagnetic wave suffers from more severe free-space loss and blockage, substantially degrading the signal-to-interference-plus-noise ratio (SINR). To remedy this shortcoming issue, multi-beam antennas (MBAs) [3] are an optimal solution since they can generate a number of

concurrent but independent directive beams with a high gain value to cover a predefined angular range. There exist two ways to realize an MBA: the phased array [3], [4] where an antenna array of N antennas is fed through a power divider from 1 to N with a controlled phase shifter on each path, or the beam forming network (BFN) [5], [6], [7], [8], [9] where an antenna array of N antennas is offering multi-beams by alternatively selecting the input excitation. The first one is efficient but redundant, and it increases the complexity of the system, whereas the second one reduces that complexity. The BFN may be digital or analog [5], among which a lot of well-known solutions such as the Rotman lens [6], the Blass matrix [7], the Nolen matrix [8], or the Butler matrix (BM) [9]. The Nolen and the Blass matrices may suffer from a lack of symmetry, leading to a potentially strong imbalance in propagation loss. The Rotman lens, preferred for mm-wave imaging applications, usually suffers from low efficiency due to high coupling between adjacent ports. On the contrary, the BM is a corporate multiple-beam feed, and it has unique

The associate editor coordinating the review of this manuscript and approving it for publication was Mohammad Tariqul Islam .

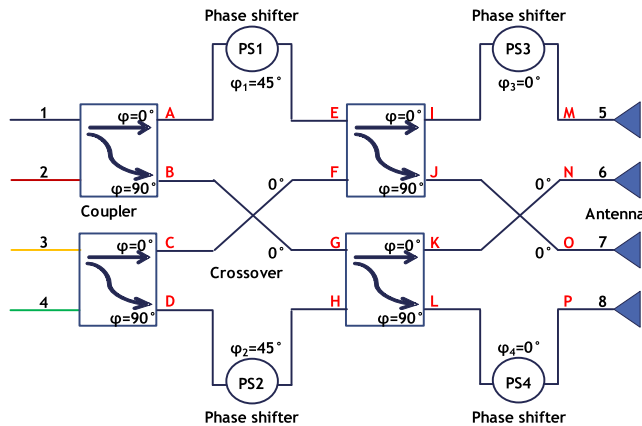


FIGURE 1. The conventional BM which sensitivity is under study.

properties as perfect matching, isolation, and equal power division, that can be obtained at the same time. The conventional BM architecture is illustrated on FIGURE 1.

Moreover, compared with the other BFNs, BM has some attractive features such as the realizable bandwidth, a structural simplicity and very low current consumption, limited to input switching purposes between ports 1 to 4. On the other hand, it has some drawbacks that are mainly related to the number of couplers and crossovers that drastically increases as the number of radiating elements raises. As explained in [10], this downside can be mitigated by using switchable phase shifters instead of the fixed ones reported on FIGURE 1. This approach leads to more degrees of freedom, allowing to achieve a flexible, progressive phase difference (PPD) at the outputs without increasing the matrix size. For example, by considering four 2-state switchable phase shifters (PS1 to PS4) and choosing proper values of the switchable phase shifts, eight switched beam configurations, similar to those achievable with an 8×8 BM, could be generated in [10], with a 4×4 BM while reducing the size up to 80%.

The BM performance is strongly related to its building blocks, whose performance is in turn affected by the selected technology and design options. In this paper, an in-depth sensitivity study carried out on each block of the BM is reported. Analytical results and full-wave simulations and measurements will demonstrate that the crossover performance is of chief importance to preserve the Butler matrix operation in terms of phase and amplitude imbalance.

Concerning practical implementation in a printed-circuit-board (PCB) technology, microstrip-based BM can be integrated into either a single-layered or multi-layered substrate. In [11] and [12], a miniaturized BM using 3-dB cross-slotted patch hybrids and a BM using only microstrip couplers and crossovers were proposed in a single-layered substrate. Unfortunately, as briefly discussed in [13], when crossovers are implemented as a tandem connection of two couplers in a single-layered configuration, a stronger amplitude and phase output signals imbalance is generated. This observation is of major importance and must be studied in detail. Multi-

layered microstrip lines were used for designing three 4×4 BMs, [13], [14], [15] and one 8×8 BM [16]. In [13], a new technique for the realization of a center crossover together with 45° phase shifters was proposed, while in [16] the double-layer structure was adopted to place components on the top and bottom layers without using any crossover. Even if not claimed, this work was enabling a BM performance improvement by avoiding crossover lack of isolation.

Alternatively, thanks to their high Q-factor, high-power capability, low-loss, and high electromagnetic compatibility, the interest in substrate integrated waveguides (SIW) has been booming since the last two decades. Several SIW BM were presented [17], [18], [19] even though, to the authors' knowledge, the building blocks effect on the BM performance was not studied in detail. Specifically, [18] reports the general trends for SIW BM in single layer PCB and it was taken as a reference for the various BM blocks in this topology. [19] provides an SIW alternative with a two-layer PCB inherently showing an infinite isolation between crossover paths. Their excellent BM performance will confirm the sensitivity study and particularly the crossover isolation impact.

The aim of this work is twofold. First, a comprehensive sensitivity study carried out on each block of the BM is reported. Analytical results, full-wave simulations and measurements are presented to demonstrate for the very first time that the crossover performance is of chief importance to preserve the Butler matrix operation in terms of phase and amplitude imbalance. Second, based on the sensitivity study outcomes, a 4×4 extended beam BM is implemented in SIW technology, which have never been proposed up to now. The approach is based on [10] and the extended beam concept is implemented at 28 GHz that is well suited to address low-cost narrow-band 5G beamforming applications. The design does not include switches yet but serves as a proof-of-concept of both the general sensitivity study carried out in this paper and the 28-GHz extended beam implementation capabilities in a low-cost PCB.

The organization is as follows. In section II, the sensitivity analysis performed using the Monte Carlo (MC) approach is used to highlight the impact of each sub-circuit of a conventional 4×4 BM (couplers, crossovers, phase shifters) on its output performance. In section III, SIW short-slot crossovers, short-slot couplers and phase-shifters are fabricated in PCB technology at 28 GHz as well as an SIW extended beam BM in two configurations as a proof-of-concept. The adopted extended beam concept is addressed along with the design blocks and experimental results are provided as well. In section IV, a discussion based on state-of-art comparison is engaged to highlight the needs for highly isolated crossovers thus confirming the sensitivity study. The array pattern is finally shown and discussed in section V. Conclusions are given in section VI.

II. SENSITIVITY STUDY OF THE 4×4 BUTLER MATRIX

The BM at hand is represented in FIGURE 1. It includes 4 couplers, 2 crossovers, and 4 phase shifters where PS1 and

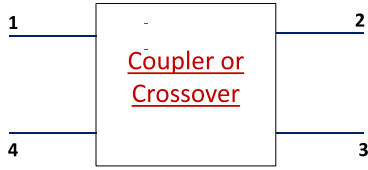


FIGURE 2. Coupler or crossover ports definition.

PS2 have a 45° phase shift while PS3 and PS4 provide a null phase shift in the conventional BM. The phases in black correspond to the absolute phase shifts induced by each block without any offset due to technical implementation.

The MC method is carried out using ADS by Keysight. It consists of performing a series of trials from randomly generated yield variable values according to statistical distribution specifications. The weakness of this method is that a full network simulation is required for each trial and that a large number of trials is required to obtain high confidence and an accurate estimate of yield. The simulator uses specific techniques to significantly boost the efficiency of the method as in [20] while maintaining its generality. Here a uniform distribution with 2000 iterations has been considered.

The process has been applied separately to each building block to figure out which component is causing the most significant imbalance or deviation between two BM output ports. On the basis of the port definition given in FIGURE 1, two main characteristics were retained. The first one is the maximum absolute amplitude imbalance considered between adjacent or non-adjacent output ports as defined in (1). The second one is the maximum absolute deviation around the progressive phase difference, PPD, taken between two adjacent output ports as defined in (2).

$$|max.out.amp.imb| = \max_{(i,k) \in \{5,6,7,8\}^2, j \in \{1,2,3,4\}, i \neq j, i \neq k, k \neq j} (|S_{ij}| / |S_{kj}|) \quad (1)$$

$$|max.out.PPDdev.| = \max_{j \in \{1,2,3,4\}} \left(\begin{array}{l} | \angle S_{8j} - \angle S_{7j} | - PPD_j \\ | \angle S_{7j} - \angle S_{6j} | - PPD_j \\ | \angle S_{6j} - \angle S_{5j} | - PPD_j \end{array} \right) \quad (2)$$

where $PPD_1 = -45^\circ$, $PPD_2 = +135^\circ$, $PPD_3 = +45^\circ$, $PPD_4 = -135^\circ$

Couplers, crossovers, and phase shifters of FIGURE 1. are hence analyzed with a specific focus on the crossover. As shown in FIGURE, a clockwise port definition is adopted for coupler or crossover.

A. MONTE CARLO ANALYSIS

1) COUPLERS IMPACT

First, the impact on the BM performance of the coupler matching, isolation, output amplitude imbalance and phase deviation were evaluated. Deviations are considered as identical for all the four couplers as they mainly depend on technological process variation. For this analysis, ideal crossovers and phase shifters are taken into account. FIG-

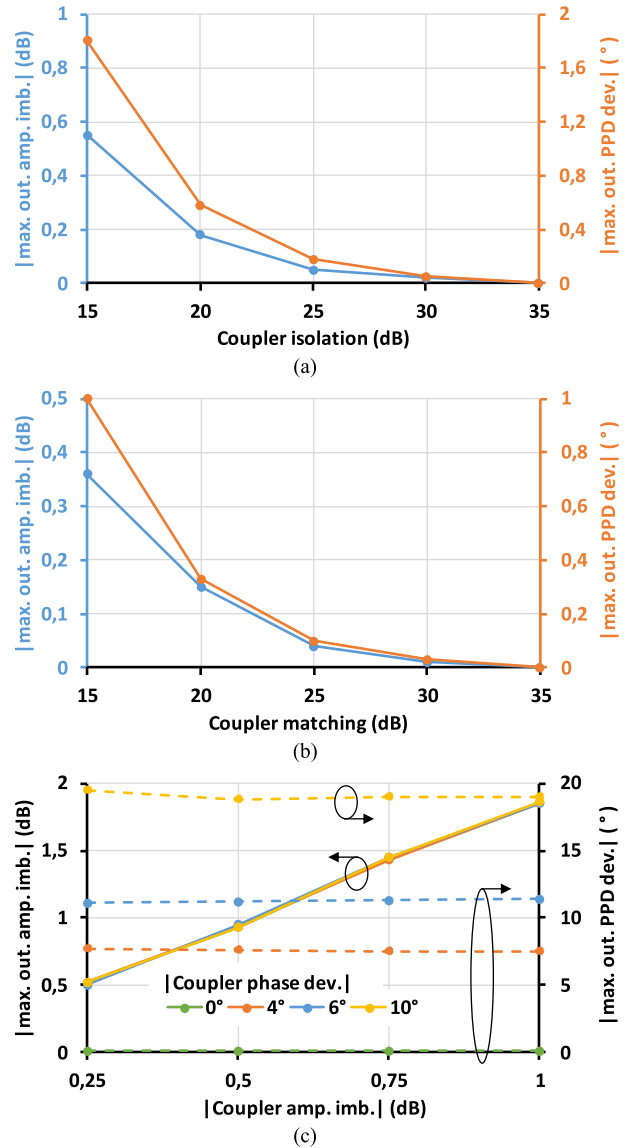


FIGURE 3. BM maximum output amplitude imbalance and PPD deviation, for couplers a) isolation, b) matching, c) amplitude imbalance and phase deviation.

URE 3 (a) shows a weak impact of reflection path isolation, i.e. S_{41} , considered as the only non-ideal parameter, i.e. less than 0.2 dB and 0.6° for $S_{41} = -20$ dB. The reflection path isolation is not the major parameter. Similarly, return loss has a negligible impact, as shown in FIGURE 3 (b), as long as return losses remain below 20 dB.

Next, while considering ideal matching and isolation, the phase and amplitude of the coupler outputs are made deviate. There are several ways to consider those deviations from the ideal case. For the case at hand, the simulation is carried out so that the phase deviation for a coupler represents the difference between the opposite, identical in modulus, phase variations around the two references 0° at node A and -90° at node B, in FIGURE 1. (C-D, I-J, K-L, respectively), corresponding to ports 2 and 3 in FIGURE 1. Concerning the amplitude

imbalance, it is automatically calculated using ADS where it was created a dedicated coupler block so that power budget, perfect input matching and isolation are idealized while imposing the targeted amplitude imbalance between nodes A and B (C-D, I-J, K-L, respectively). Results are represented on FIGURE 3 (c). When the coupler amplitude imbalance is varied between 0 and ± 1 dB, twice the value is observed on the BM maximum output amplitude imbalance, whatever the coupler phase deviation. Similarly, variations in the coupler output phases induce only BM output phase imbalance changes. A BM maximum absolute PPD deviation as high as $19\text{-}20^\circ$ might be observed when a coupler phase deviation of $\pm 10^\circ$ is applied.

B. CROSSOVERS IMPACT

A similar study showing the impact of mismatching and lack of isolation is performed for the crossovers. In this case, the couplers and PSs are considered as ideal components.

FIGURE 4 (a) shows a weak impact of the crossover reflection path isolation, i.e. S_{41} of FIGURE 1. Provided that reflection path isolation is better than 20 dB, the resulting BM amplitude imbalance does not exceed 0.3 dB, and negligible impact on the phase is observed. Similarly, return loss has little impact on FIGURE 4 (b).

Lastly, the impact of the crossover transmission path isolation, i.e. S_{21} of FIGURE, associated to the phase deviation, is considered, any other parameters being ideal. Here, the simulation is carried out so that the phase deviation for a crossover represents the difference between the opposite, identical in modulus, phase variations around the two references 0° at node F and 0° at node G, in FIGURE 1 (N-O, respectively), corresponding to ports 2 and 3 in FIGURE 2. As shown in FIGURE 4 (c), the impact of crossover transmission path isolation S_{21} on the BM output performance is high whatever the crossover phase deviation. When transmission path isolation deteriorates from 35 dB down to 15 dB, the BM output maximum amplitude imbalance modulus increases from 0.35 dB to 3.7 dB (no dependency with the crossover coupled and transmission path phase variation) while the output phase imbalance modulus goes from 1.5° , better case, to 25.1° , poorer case. Besides, when considering a quite good transmission path isolation, $S_{21} = -25$ dB, the output phase imbalance modulus becomes greater than 10° whilst the crossover phase deviation is still small (6°). It must be noted that even for an excellent direct transmission path isolation of 35 dB, the BM output maximum PPD deviation modulus varies from 1.5° up to 14.5° when the crossover output phase deviation varies from 0° to 10° .

Therefore, BM operation can be significantly undermined by the crossover isolation performance. It is worth studying it in depth by providing analytical formulas that can better describe the crossover transmission path isolation sensitivity problem.

C. PHASE SHIFTERS IMPACT

In this study, the phase range of each phase shifter (PS) is varied from 0 to $\pm 5^\circ$ at nodes E, H, M and P simultaneously,

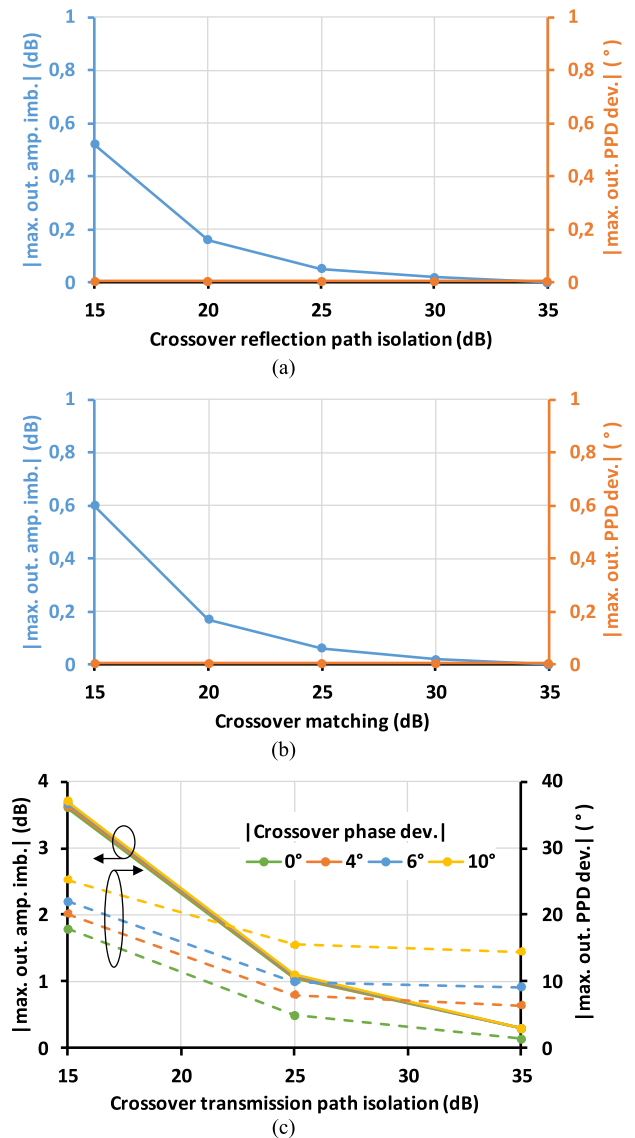


FIGURE 4. BM maximum output amplitude imbalance and PPD deviation, for crossovers a) reflection path isolation, b) matching, c) transmission path isolation and phase deviation.

the crossovers and the couplers being considered ideal. For a phase variation of $\pm 5^\circ$, an output BM phase imbalance modulus of almost 30° is obtained, as shown in FIGURE, corresponding to a phase variation at each port of $\pm 15^\circ$. As it will be shown in Section IV, this error has a limited impact on the array factor. No output BM amplitude imbalance occurs.

III. THEORETICAL ANALYSIS

In terms of modulus, it has been seen that crossovers transmission path isolation is the main parameter to be considered, impacting both BM output amplitude imbalance and PPD deviation (FIGURE 5). In parallel, phase variations at each block primarily impact the PPD. By the way, even if couplers, PSs and crossovers phase variations are also important parameters, prototypes may be improved in terms of final

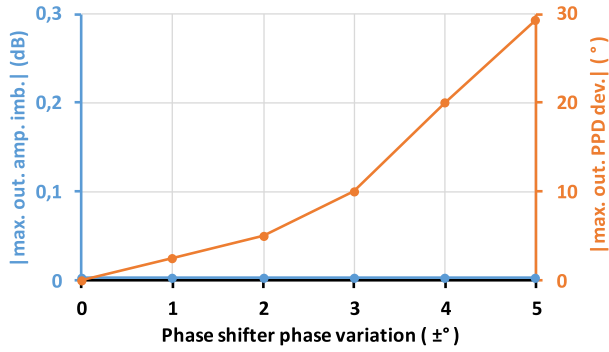


FIGURE 5. BM maximum output amplitude imbalance and PPD deviation, for PSs phase variation.

lengths by the end. In contrast, a transmission path isolation of 25 dB may be simply unreachable in the chosen technology. In this paragraph, an analytical study is proposed to illustrate the dependency of the BM performance on the crossover behaviour. Lossless circuits are considered as ideal standalone circuits except for the crossover whose S_{21} (ideally linearly null) will be varied. Hence, the following parameters are considered:

- 3dB couplers:
 - Perfect matching ($S_{11} = S_{22} = S_{33} = S_{44} = 0$)
 - Perfect isolation ($S_{41} = 0$),
 - No output phase variation or amplitude imbalance:

$$(S_{21} = T \cdot e^{j0} = T = \frac{1}{\sqrt{2}})$$

$$(S_{31} = \sqrt{1 - T^2} \cdot e^{-j\frac{\pi}{2}} = -j\sqrt{1 - T^2} = -j\frac{1}{\sqrt{2}})$$

- Phase shifters:
 - Perfect matching ($S_{11} = S_{22} = 0$)
 - No phase error ($S_{21} = e^{-j\varphi_i}$)
- Crossovers:
 - Perfect matching ($S_{11} = S_{22} = S_{33} = S_{44} = 0$)
 - Perfect reflection path isolation between port 1 and 4 ($S_{41} = 0$),
 - Coupling parameter ($S_{31} \neq 1$) leading to a non-ideal transmission path isolation parameter ($S_{21} \neq 0$):

$$(S_{21} = \varepsilon \cdot e^{+j\frac{\pi}{2}} = j\varepsilon)$$

$$(S_{31} = \sqrt{1 - \varepsilon^2} \cdot e^{j0} = \sqrt{1 - \varepsilon^2})$$

The study is performed at one fixed frequency under two cases, port 1 or port 2 feeding the BM. It is unnecessary to study ports 3 or 4 feeding due to symmetry.

1) PORT 1 FEEDING

Reduced power waves are considered at the outputs of FIGURE 1, resulting in (3), as shown at the bottom of the next page.

Equation (1) is then simplified to (4), recalling that $\varphi_3 = \varphi_4 = 0^\circ$ in conventional matrices and that $T = \sqrt{1 - T^2} =$

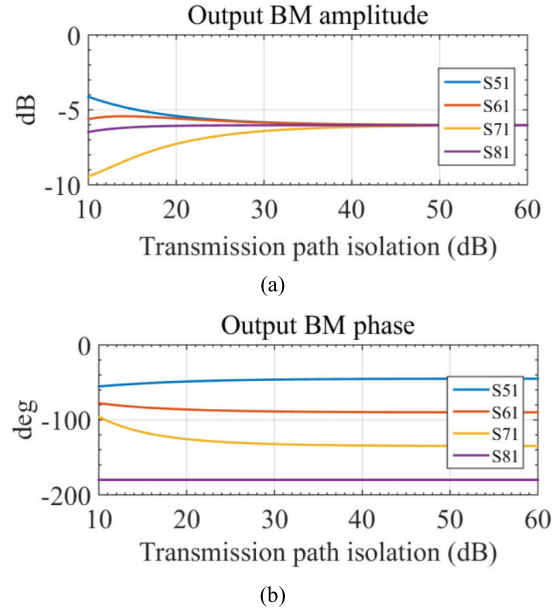


FIGURE 6. BM S-parameters a) amplitude and b) phase when port 1 is fed.

$$\frac{1}{\sqrt{2}}.$$

$$\Leftrightarrow \begin{cases} b_5 = T^2(e^{-j\varphi_1} + e^{-j\frac{\pi}{2}} \varepsilon) \\ b_6 = T^2 \left(e^{-j\frac{\pi}{2}} + \varepsilon \left(e^{-j\varphi_1} + 2\varepsilon e^{j\frac{\pi}{2}} \right) \right) \\ b_7 = T^2 \left(e^{j(-\varphi_1 - \frac{\pi}{2})} + 2\varepsilon \right) \left(\sqrt{1 - \varepsilon^2} \right) \\ b_8 = -T^2 \left(\sqrt{1 - \varepsilon^2} \right) \end{cases} \quad (4)$$

Remark: if $\varepsilon = 0$ and for $\varphi_1 = 45^\circ$, the conventional BM phase shifts are recovered:

$$\Leftrightarrow \begin{cases} b_5 = T^2(e^{-j\varphi_1}) \rightarrow \text{phase shift of } -45^\circ \\ b_6 = T^2 e^{-j\frac{\pi}{2}} \rightarrow \text{phase shift of } -90^\circ \\ b_7 = T^2 \left(e^{j(-\varphi_1 - \frac{\pi}{2})} \right) \rightarrow \text{phase shift of } -135^\circ \\ b_8 = -T^2 \rightarrow \text{phase shift of } -180^\circ \end{cases} \quad (5)$$

The S-parameters of the resulting system are plotted in amplitude and phase on FIGURE 6.

2) PORT 2 FEEDING

Similarly, it can be shown that:

$$\Leftrightarrow \begin{cases} b_5 = T^2(e^{j(-\varphi_1 - \frac{\pi}{2})} + \varepsilon) \\ b_6 = T^2 \left(1 + \varepsilon \left(e^{j(-\varphi_1 - \frac{\pi}{2})} - 2\varepsilon \right) \right) \\ b_7 = T^2 \left(e^{j(-\varphi_1 - \pi)} + 2\varepsilon e^{j\frac{\pi}{2}} \right) \left(\sqrt{1 - \varepsilon^2} \right) \\ b_8 = \left(T^2 e^{-j\frac{\pi}{2}} \right) \left(\sqrt{1 - \varepsilon^2} \right) \end{cases} \quad (6)$$

Remark: if $\varepsilon = 0$ and for $\varphi_1 = 45^\circ$, the conventional BM phase shifts are recovered:

$$\begin{aligned} b_5 &= T^2 \left(e^{j(-\varphi_1 - \frac{\pi}{2})} \right) \rightarrow \text{phase shift of } -135^\circ \\ b_6 &= T^2 \rightarrow \text{phase shift of } 0^\circ \end{aligned}$$

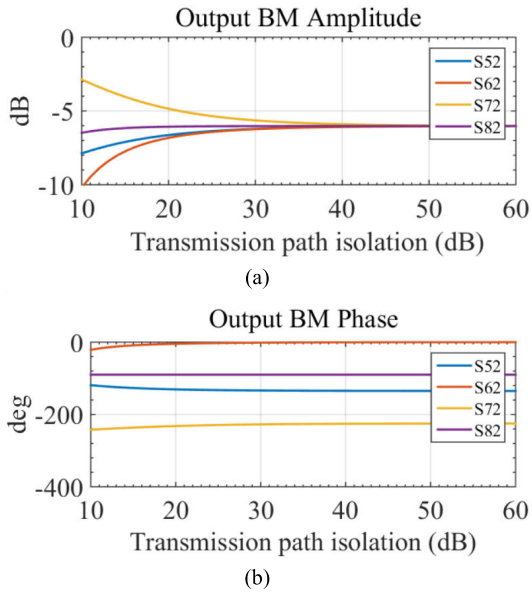


FIGURE 7. BM output a) amplitude and b) phase when port 2 is fed.

$$\begin{aligned}
 b_7 &= T^2 \left(e^{j(-\varphi_1 - \pi)} \right) \rightarrow \text{phase shift of } -225^\circ (= +135^\circ) \\
 b_8 &= T^2 e^{-\frac{j\pi}{2}} \rightarrow \text{phase shift of } -90^\circ (= +270^\circ)
 \end{aligned} \quad (7)$$

The S-parameters of the resulting system are plotted in amplitude and phase on FIGURE 6.

3) DISCUSSION

As it can be observed in FIGURE 7, for a crossover transmission path isolation of 15 dB, the BM output amplitude imbalance is almost equaling 4 dB, whatever is the feeding port as predicted by the MC analysis. It is worth noticing that S_{81} (S_{82} respectively) remains almost unchanged. More generally, by considering the four S-parameters, for a 30 dB crossover output path isolation, the BM output amplitude imbalance modulus is 0.59 dB (0.6 dB, respectively) and the BM output phase imbalance modulus is 2.7° (2.6°, respectively) when port 1 (port 2, respectively) is fed, which has a limited impact on an antenna array pattern. Anyway 30 dB may be difficult to reach, at the state-of-art. In practice, the BM designers should pay attention to the implementation of the crossover before designing BM because its transmission

path isolation might dramatically spoil the performance of the overall system, if its value is not high enough.

IV. VALIDATION

The design of a SIW Butler matrix at 28 GHz is presented in this section, taking advantage of the extended beam concept. As the number of blocks is identical, whatever the chosen phase shift value for PS1, PS2, PS3, or PS4, the sensitivity study keeps valid with a strong impact of the crossover isolation on BM outputs mismatch. After justifying the interest for the extended beam, a specific focus will be given to the crossover design before showing the extended beam BM measured results.

A. MATRIX DESIGN

In many current applications, high beam resolution becomes unavoidable. One way to enhance spatial resolution is to increase the order of the BM, but the circuit size would become impractically large. Thus, one of the most interesting features can be to extend the beam-steering ability. Several techniques were reported in the literature [21], [22], [23], [24], [25]. In this work, tunable phase shifters are considered. Even if not inspired, this concept is similar to the one recently published in [10] and is applied, in our case, to a higher frequency, 28 GHz. This design provides the 4×4 BM with extra beam control agility, along with a wide equivalent spatial coverage having high peak gain and low gain ripple. The solution proposed in this document is to replace the two 45° and two 0° fixed PSs of FIGURE 1. by four tunable 1-bit PSs, depicted in FIGURE 8. The proposed design does not add a lot of extra power loss compared to the 4×4 BM design, and enables much less complexity and loss than the 8×8 BM. The maximum beam radiation intensity direction depending on the phase shifters state is summarized in Table 1. To better figure out the principle, let us consider the example of port 1 feeding (first line of Table 1). If PS1 is on path 1 (0° phase shift), PS3 on path 2 (90° phase shift) and PS4 on path 2 as well (270° phase shift), then the progressive output phases is equal to 0° and, in turns, a boresight beam is obtained. PS2 is not considered here because it is not in the signal path. The same principle is valid for the other combinations to obtain by the end height possible progressive phase differences, PPDs, i.e. nine possible beam directions, θ , as summarized in Table 1.

$$\left[\begin{array}{l}
 b_5 = T(e^{-j\varphi_1})T(e^{-j\varphi_3}) + \left(\sqrt{1-T^2}e^{-\frac{j\pi}{2}}\right) \left(\varepsilon e^{\frac{j\pi}{2}}\right) \left(\sqrt{1-T^2} \cdot e^{-\frac{j\pi}{2}}\right) (e^{-j\varphi_3}) \\
 b_6 = T e^{-j\varphi_1} \left(\sqrt{1-T^2}e^{-\frac{j\pi}{2}}\right) \left(\varepsilon e^{\frac{j\pi}{2}}\right) + \left(\sqrt{1-T^2}e^{-\frac{j\pi}{2}}\right) \left(\left(\varepsilon e^{\frac{j\pi}{2}}\right) T \left(\varepsilon e^{+\frac{j\pi}{2}}\right) + \left(\sqrt{1-\varepsilon^2}\right) T \left(\sqrt{1-\varepsilon^2}\right)\right) \\
 b_7 = T(e^{-j\varphi_1}) \left(\sqrt{1-T^2}e^{-\frac{j\pi}{2}}\right) \left(\sqrt{1-\varepsilon^2}\right) + \left(\sqrt{1-T^2}e^{-\frac{j\pi}{2}}\right) \left(\left(\varepsilon e^{\frac{j\pi}{2}}\right) T \left(\sqrt{1-\varepsilon^2}\right) + \left(\sqrt{1-\varepsilon^2}\right) T \left(\varepsilon e^{+\frac{j\pi}{2}}\right)\right) \\
 b_8 = \left(\sqrt{1-T^2}e^{-\frac{j\pi}{2}}\right) \left(\sqrt{1-\varepsilon^2}\right) \left(\sqrt{1-T^2}e^{-\frac{j\pi}{2}}\right) (e^{-j\varphi_4})
 \end{array} \right] \quad (3)$$

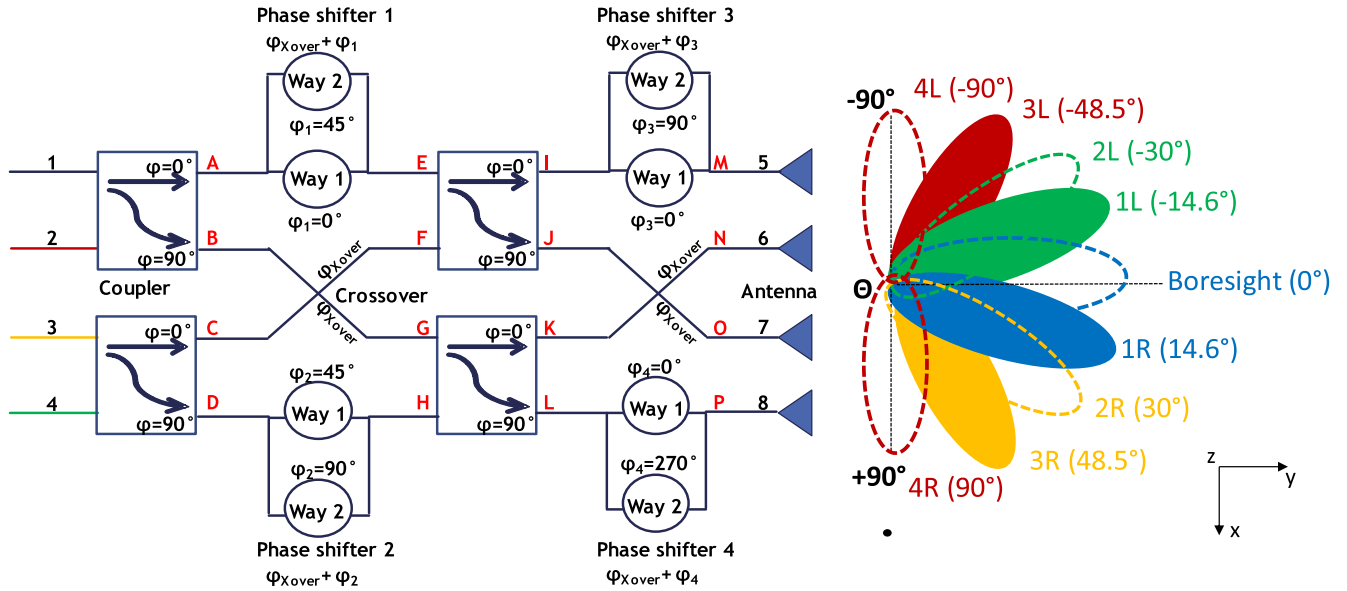


FIGURE 8. Extended beam BM network concept based on reconfigurable phase shifters. The phases at the outputs of the couplers correspond to the absolute phase shifts induced by those blocks, in an ideal extended beam BM, without any offset due to technical implementation.

TABLE 1. Extended beam BM combinations for enhanced spatial agility.

Port	BM	PS 1		PS 2		PS 3		PS 4		PPD (°)	θ (°)
		Way 1 φ ₁ = 0°	Way 2 φ ₁ = 45°	Way 1 φ ₂ = 45°	Way 2 φ ₂ = 90°	Way 1 φ ₃ = 0°	Way 2 φ ₃ = 90°	Way 1 φ ₄ = 0°	Way 2 φ ₄ = 270°		
1	BM1	ON	OFF	n/p	n/p	OFF	ON	OFF	ON	0	0
	BM2	OFF	ON	n/p	n/p	ON	OFF	ON	OFF	-45	14.6
2	BM1	ON	OFF	n/p	n/p	OFF	ON	OFF	ON	±180	±90
	BM2	OFF	ON	n/p	n/p	ON	OFF	ON	OFF	135	-48.5
3	BM1	n/p	n/p	OFF	ON	OFF	ON	OFF	ON	-90	30
	BM2	n/p	n/p	ON	OFF	ON	OFF	ON	OFF	-135	48.5
4	BM1	n/p	n/p	OFF	ON	OFF	ON	OFF	ON	90	-30
	BM2	n/p	n/p	ON	OFF	ON	OFF	ON	OFF	45	-14.6

Any circuit was designed and then fabricated on Roger substrate with thickness, ε_r and tanδ of 0.813 mm, 3.55 and 0.0027.

B. CROSSOVER

The short-slot technique is a well-suited topology for BM coupler and crossover realized in a PCB-SIW technology. It was first introduced by Riblet in 1950 [26] along with its theoretical description, and described in SIW technology by Chen in [18]. Basically, its operation principle relies on the interference of two propagating modes. For practical reasons, the accesses operate in their mono-mode frequency band, carrying only a propagating TE₁₀. An enlarged middle section is inserted between the four waveguide accesses where both TE₁₀ and TE_n20 modes can propagate and interfere, thus providing the power division functionality. A picture of the fabricated short-slot crossover along with E-field simulated through HFSS software is depicted in FIGURE 9. The dimensions are summarized in Table 2. After optimization, the crossover width, W_{cavity}, is equal to 7.75 mm, leading to the

TABLE 2. Crossover dimensions.

D (mm)	p (mm)	W _{cavity} (mm)	L _{cavity} = L _{Xover} (mm)	Δ _{access} (mm)	L (mm)	Total length (mm)*	Total width (mm)*
0.2	0.45	7.75	11.72	1	9	13.72	9.66

*without feeding lines

best transmission path isolation of 30 dB. For comparison W_{Xover} equal to 7.6 or 7.9 mm, with same length deteriorates isolation to around 25 dB.

Measurements were performed on an Anritsu 145-GHz ME7838D4 4-port VNA vector network analyser calibrated through SOLT standards. The G-CPW to SIW feeding accesses were de-embedded by using TRL calibration samples [27]. The amplitude and phase results are shown in FIGURE 10, between 23 GHz and 31 GHz.

The measurements (solid lines) are plotted and compared with simulations (dotted lines). As it can be noticed, the measurements are in good agreement with simulations. The

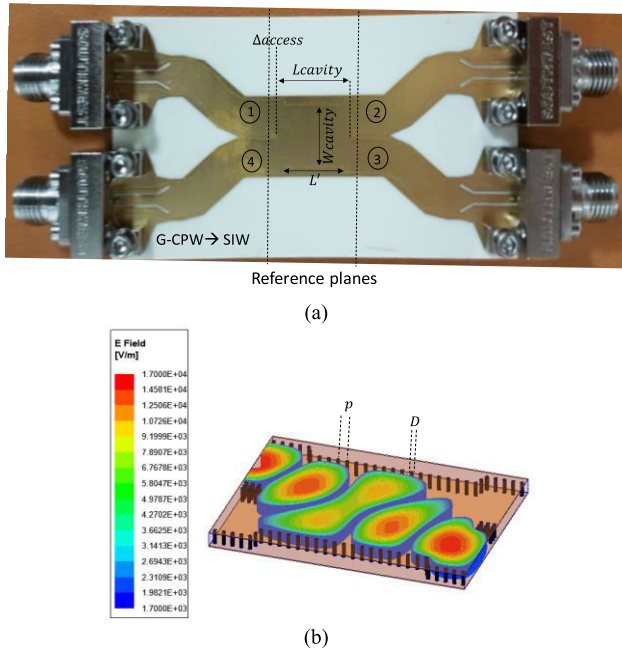


FIGURE 9. Short-slot SIW crossover: (a) implemented crossover with G-CPW accesses. Short-slot SIW coupler benefits from the same topology but with proper L_{cavity} (and consequently L) (b) Crossover simulated E-field.

TABLE 3. Coupler dimensions.

D (mm)	p (mm)	W_{cavity} (mm)	$L_{cavity} =$ $L_{coupler}$ (mm)	Δ_{access} (mm)	L (mm)	Total length (mm)*	Total width (mm)*
0.2	0.45	7.75	5.48	1	9	7.48	9.66

*without feeding lines

measured insertion loss is 0.5 dB, at 28 GHz, while reducing by 1 dB between 23.5 GHz up to 30.7 GHz (25.7% of relative BW, RBW). The return loss and reflection path isolation are 23.5 dB and 29.8 dB at 28 GHz, respectively; the return loss remains better than 10 dB between 20.1 GHz and 30.1 GHz (35.7% of RBW), while the reflection path isolation is better than 10 dB between 23.4 GHz and 31.2 GHz (27.9% of RBW). The level of transmission path isolation is very important, as aforementioned, it remains below 30 dB between 26.3 and 30 GHz, which represents a very good result (13.2% of RBW). The measured phase of S_{31} is equal to -78.5° at 28 GHz, and it remains within $\pm 10^\circ$ only between 27.75 GHz and 28.25 GHz (1.8% of RBW). That shows a quite big dispersion of the device. The aforementioned absolute phase is very important, because all the phase shifters (introduced in the next section) were designed according to this value, so that the output BM phase imbalance is eventually minimized.

C. COUPLERS

The short-slot 3-dB coupler was realized with the same technique as for crossover (see FIGURE 9) but with a

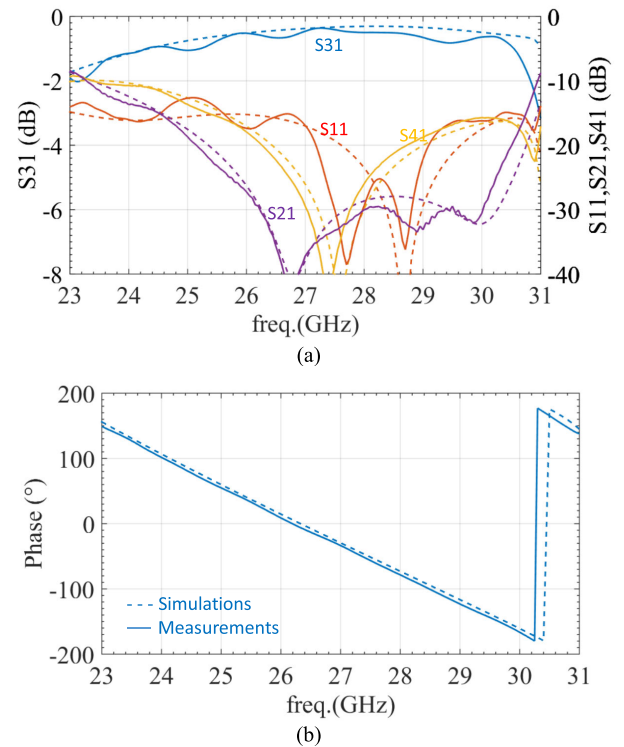


FIGURE 10. Short-slot crossover measured and simulated results: (a) amplitude, (b) phase. De-embedded measurements (straight line), simulations (dotted lines).

shorter length $L_{Coupler}$ resulting in total dimensions of 7.48 mm \times 9.66 mm. The optimizations of the coupler dimensions, as reported in Table 3, resulted in a low measured IL of 0.25 dB at 28 GHz, as shown in FIGURE 11. Return loss and isolation are lower than 30 dB at 28 GHz, and the relative bandwidth for a 10 dB matching equals 26.8%. Output amplitude and phase imbalances are as low as 0.1 dB and 2.3° , respectively, at 28 GHz. Accordingly to FIGURE 11, this should only affect phase imbalance.

D. PHASE SHIFTERS FOR IMPLEMENTATION IN AN EXTENDED BEAM 4 \times 4 BM

The design approach falls within the digital switched line topology where floating vias are connected to the upper and/or bottom plates of the SIW through PIN diodes. Besides phase shifters [28], [29], a similar technique was used for different SIW devices, e.g. antennas [30], [31], [33], filters [34] and switches [35], [36]. In our proper case, PIN diodes got replaced by metal strips as a proof-of-concept.

PS4 is the most intuitive case. The principle of the phase shifter consists in routing the EM wave towards one over two possible paths, way 1 and way 2, by enabling (ON) or disabling (OFF) floating vias. The principle was introduced in [37] for a single pole double throw and adapted here to phase shifting. The “ON” vias act as electromagnetic walls. On the contrary, the “OFF” vias let the EM wave pass through the SIW. Thus, two absolute phases and a relative phase shift are

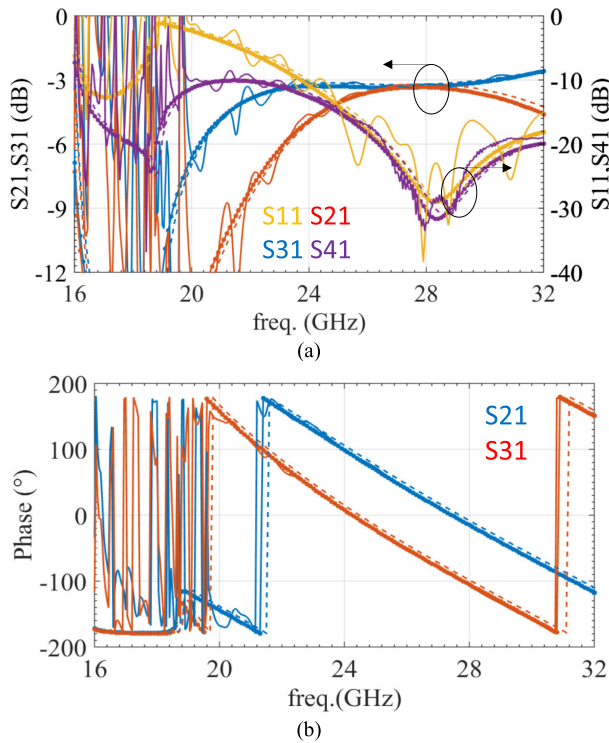


FIGURE 11. Short-slot coupler measured and simulated results: (a) amplitude, (b) phase. De-embedded measurements (straight line), simulations (dotted lines).

generated. In FIGURE 12, in BM1, port1 or port 2 feeding as an example, the way 2 of PS4 (on the bottom right) is always favored ($348^\circ = \varphi_{Xover} + \varphi_4 = 78^\circ + 270^\circ$ as in Table 1) whereas, in BM2, port 1 or port 4 feeding as an example, the way 1 of PS4 is always activated ($78^\circ = \varphi_{Xover} + \varphi_4 = 78^\circ + 0^\circ$ as in Table 1).

For PS1, PS2 and PS3, concerned by smaller phase differences between ways 1 and 2, and contrarily to PS4, it was not possible to design two parallel physical paths because of the technology constraints. Theoretically speaking, the design principle is straightforward and is inspired from [38] although in [38] waveguides are not switchable but juxtaposed. The phase change is due to an inherent property of the rectangular waveguides for which cut-off frequency depends on their width. In the meantime, whatever the width, the slope of the phase constant, $\beta(f)$, as a function of frequency, f , stays the same, so that, at a given frequency, β is finally higher for bigger widths. This physical propriety is very suited to perform phase shifting.

Practically speaking, phase shifters PS1, PS2 and PS3 are designed the following way. On the basis of the crossover physical length, the respective length of PS1, PS2, and PS3 are bent to obtain 78° , 123° , and 78° of phase shift in way 1 configuration ($\varphi_{Xover} + \varphi_{1,2,3-way 1} = 78^\circ + 0^\circ, 45^\circ, 0^\circ$ respectively as in Table 1). This phase shift corresponding to way 1 is obtained for a given SIW width. If four rows of floating vias are available, as it is the case for PS3 on the

TABLE 4. Simulated phase shifters results at 28 GHz.

PS	Φ way1 ($^\circ$) (ideal)	IL way1 (dB)	Φ way2 ($^\circ$) (ideal)	IL way2 (dB)
PS1	78.8 (78 $^\circ$)	0.56	120.1 (123 $^\circ$)	0.66
PS2	122.7 (123 $^\circ$)	0.64	165.4 (168 $^\circ$)	0.77
PS3	76.2 (78 $^\circ$)	0.72	168.4 (168 $^\circ$)	1
PS4	75.6 (78 $^\circ$)	0.89	345.8 (348 $^\circ$)	1.13

right top of FIGURE 12, it is enough to put metal strips (“ON vias”) on the adequate set of rows while letting the two others floating, in order to get the targeted width corresponding to the targeted β , thus favoring the targeted way 1 or way 2. As a consequence, in way 2 configuration, the signal phase will be delayed up to 123° , 168° and 168° for PS1, PS2 and PS3, respectively ($\varphi_{Xover} + \varphi_{1,2,3-way 2} = 78^\circ + 45^\circ, 90^\circ, 90^\circ$ respectively, as in Table 1). In FIGURE 12, in BM1, port1 or port 2 feeding as an example, the way 2 of PS3 (on the top right) is always favored ($168^\circ = \varphi_{Xover} + \varphi_{3-way 2} = 78^\circ + 90^\circ$, as in Table 1) whereas, in BM2, port 1 or port 4 feeding as an example, the way 1 of PS3 is always activated ($123^\circ = \varphi_{Xover} + \varphi_{3-way 1} = 78^\circ + 45^\circ$, as in Table 1). Table 4 provides the simulated IL, matching and phase shifts for the four phase shifters. Based on the sensitivity study, FIGURE 5, and on the average phase deviations of the simulated PSs (1.67°), it may be expected some mismatch in terms of PPD no more than $|4.5^\circ|$, corresponding to a phase variation at each output BM port of $\pm 4.5^\circ/2$. That will affect the beam direction of the antenna array system in a very moderate way, as calculated in section IV. Phase shifters were fabricated (see FIGURE 13) and measured.

For each PS, two versions were tested corresponding to way 1 and way 2, respectively. This choice has been adopted as well for the final Butler matrix implementation with two configurations and enabled to demonstrate, without any need for PIN diode biasing, the two main contributions of this study, that is to say, sensitivity to crossover isolation and feasibility of an extended beam Butler matrix at 28 GHz in a conventional planar PCB technology.

FIGURE 14. compares PS simulations to measurements showing good agreement. Matching and insertion loss have been reported on FIGURE 14. (a) to (d) for the four PSs. Measured insertion loss is below 1 dB each time with an overestimation of simulated insertion loss at 28 GHz of about 0.3 dB (0.5 dB for PS3). Matching stays better than 12 dB between 26 and 30 GHz and better than 15 dB between 27.5 and 28.5 GHz. On FIGURE 14(e), the phase difference

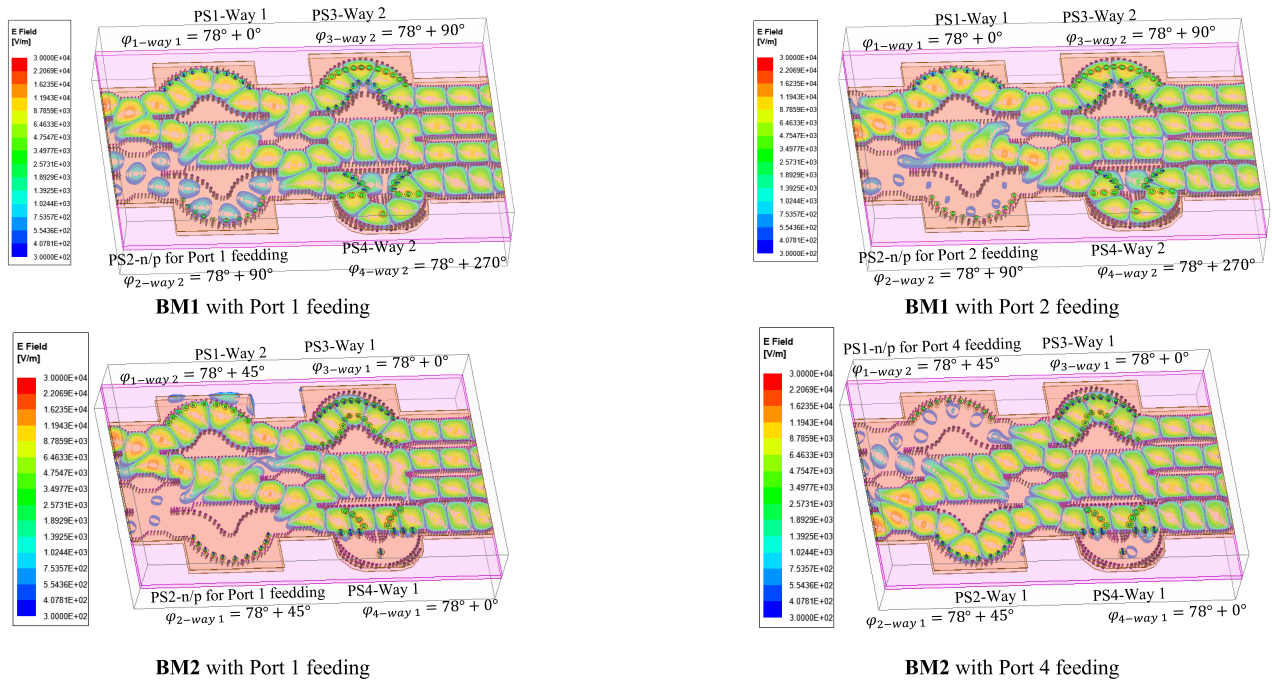


FIGURE 12. E-field for various feeding configurations of BM1 or BM2.

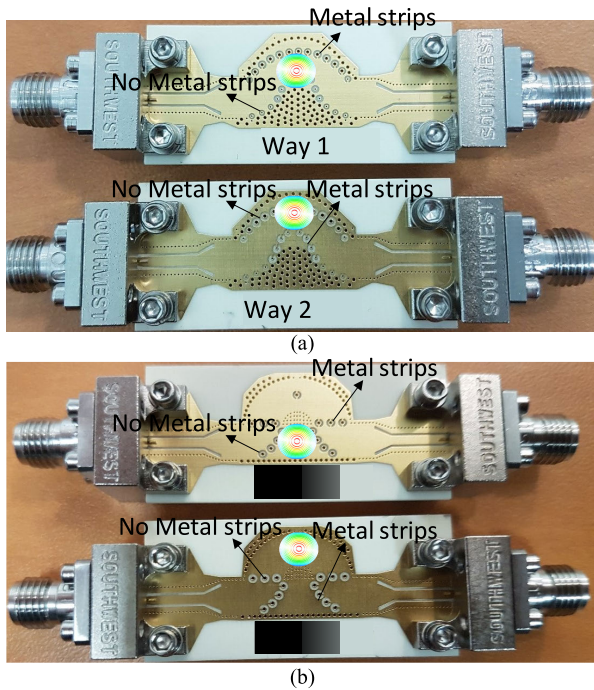


FIGURE 13. Phase shifters with two ways configuration. a) PS3. (PS1 and PS2 look similar). b) PS4.

for the four PSs shows excellent agreement for PS3, 8° of maximal deviation at 28 GHz for PS4 and -5° of maximal deviation at 28 GHz for PS1 and PS2. Between 27.5 and 28.5 GHz, PS4 phase difference varies between -2° and 18° .

In order to estimate real PIN diodes impact, MACOM MA4AGP907 devices were chosen showing 4.2Ω and 0.02 pF for *ON* and *OFF* equivalent model respectively. Simulated PS4 insertion losses were deteriorated from 0.3 to 0.7 dB in way 1 and from 0.45 to 1 dB in way 2, meaning a maximum deterioration per PS of 0.55 dB. Hence the impact on the overall Butler matrix should not exceed 1.1 dB of extra-loss as compared to the following measured ones.

E. BUTLER MATRIX MEASUREMENT RESULTS

As a proof-of-concept, the two Butler matrices described in FIGURE 15 were fabricated using the aforementioned design blocks, which provides eight different PPDs, each matrix providing four of them. As indicated previously, two Butler matrices are needed because the phase shifters are not reconfigurable and for each BM a particular combination of those must be provided, according to Table 1. To better figure out the flow of the RF signal, the HFSS E-fields of BM1 and BM2 are depicted in FIGURE 12 for some particular feeding configurations.

The BM measurement set-up is displayed in FIGURE 15. The same VNA as for the stand-alone blocks (see crossover section) was calibrated through SOLT standards. Subsequently, two TRL calibrations were performed, whose TRL samples were used to de-embed either external and internal accesses. As the only difference between the two Butler matrices is the presence or not of metal strips that are not visible at system scale, matrices look similar, and only BM1 is presented. The example of FIGURE 15 enables to measure the case of port 1 feeding or port 2 feeding. It is worth noticing

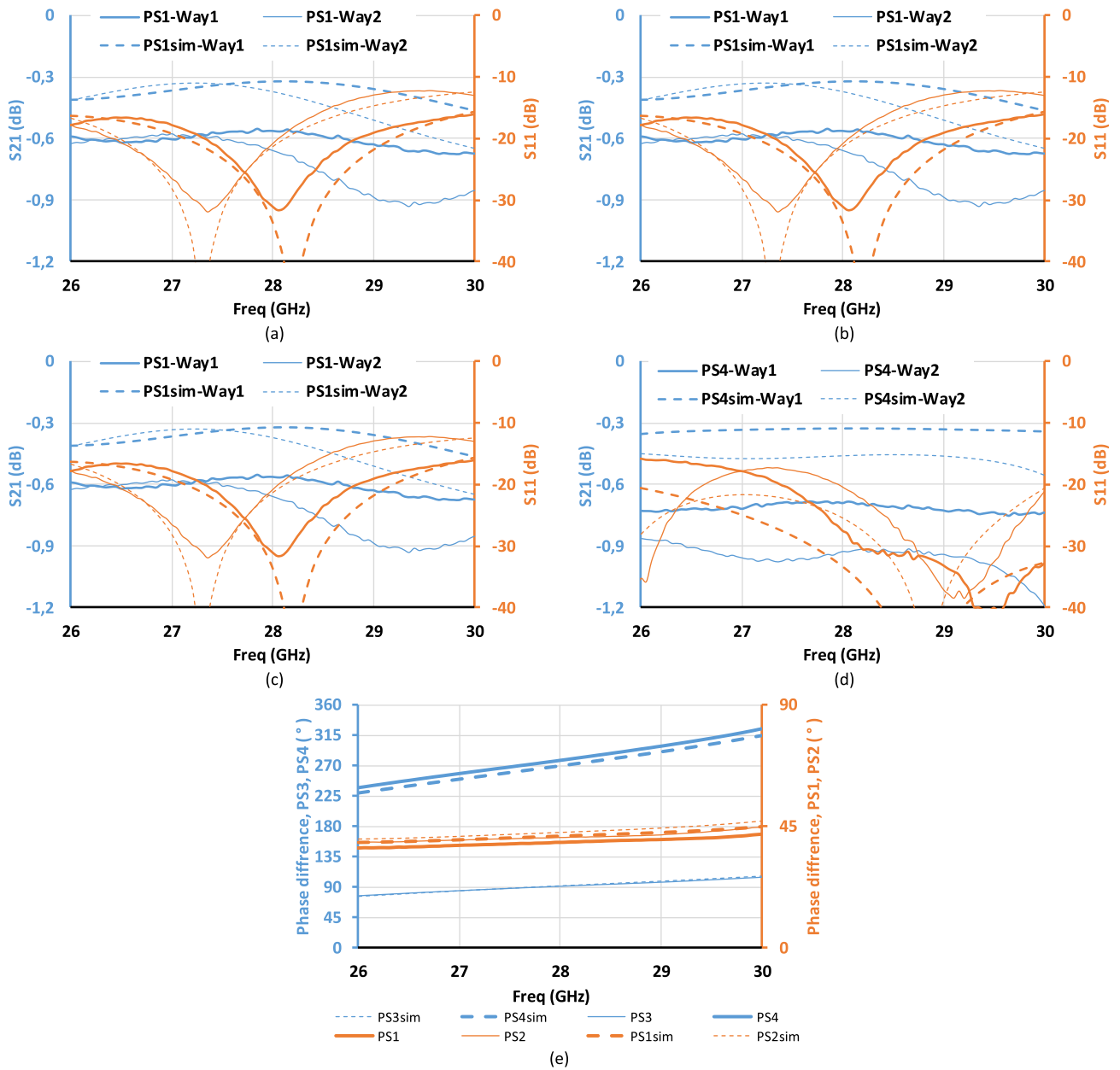


FIGURE 14. Phase shifters measurements compared to simulation results. a) PS1. b) PS2, c) PS3, d) PS4 S-parameters for ways 1 and 2. e) Phase difference between way2 and way1 for the four phase shifters. De-embedded measurements (straight line), simulations (dotted lines).

that both ports are not fed in the same time as the VNA sequentially switches the RF signal towards the two ports. Butler matrix ports 3 and 4 are not available in this configuration and have been loaded with a 50-Ohm matching load to not interfere with measurements. At the output side, only two ports can be measured over the four available ones. In the case of FIGURE 15, it can be seen they consist in ports 7 and 8 whilst ports 5 and 6 are loaded with 50 Ohm. Hence, two input matching coefficients, two isolation coefficients and four transmission coefficients can be measured in this configuration through $S_{11VNA} = S_{11BM}$ and $S_{22VNA} = S_{22BM}$, $S_{21VNA} = S_{21BM}$ and $S_{12VNA} = S_{12BM}$, $S_{31VNA} = S_{71BM}$

and $S_{41VNA} = S_{81BM}$ and $S_{32VNA} = S_{72BM}$ and $S_{42VNA} = S_{82BM}$, respectively. Four configurations per matrix are then needed in order to get the totality of the measurement.

Measurements results are presented in FIGURE 16 and summarized at 28 GHz in Table 5 for BM1, and in Table 6 for BM2. Matching is better than 17 dB between 27.5 and 28.5 GHz and isolation superior to 21 dB in the same frequency range. At 28 GHz, some mismatch occurs in the PPD with a maximum of 16.9° attained in the BM2 configuration when feeding port 2 is chosen. The maximum insertion loss is equal to 2.8 dB. The maximum amplitude imbalance equals 1.33 dB, while the mean maximum amplitude imbalance

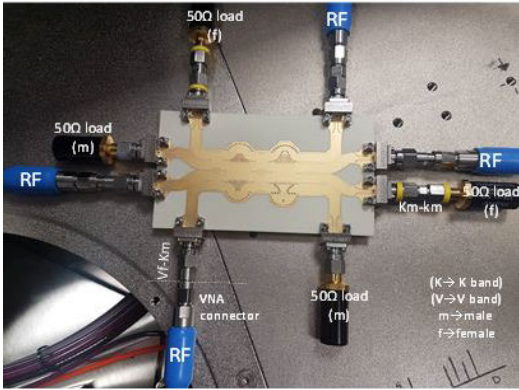


FIGURE 15. Butler matrix measurement set-up. Example on BM1.

TABLE 5. Extended beam BM1 measurements results at 28 GHz.

Port1	S_{51}	S_{61}	S_{71}	S_{81}
IL (dB)	-8.48	-7.89	-8.38	-8.13
Max amp. imb.(dB)	0.59			
PPD	$\angle S_{81} - \angle S_{71}$	$\angle S_{71} - \angle S_{61}$	$\angle S_{61} - \angle S_{51}$	
Ideal $\rightarrow 0^\circ$	$0^\circ + 10.3^\circ$	$0^\circ - 14.5^\circ$	$0^\circ + 15.4^\circ$	
Port2	S_{52}	S_{62}	S_{72}	S_{82}
IL (dB)	-8.36	-7.98	-7.96	-8.13
Max amp. imb.(dB)	0.4			
PPD	$\angle S_{82} - \angle S_{72}$	$\angle S_{72} - \angle S_{62}$	$\angle S_{62} - \angle S_{52}$	
Ideal $\rightarrow \pm 180^\circ$	$180^\circ + 15.7^\circ$	$180^\circ - 15.5^\circ$	$180^\circ + 9.2^\circ$	
Port3	S_{53}	S_{63}	S_{73}	S_{83}
IL (dB)	-8.37	-7.45	-8.54	-8.78
Max amp. imb.(dB)	1.33			
PPD	$\angle S_{83} - \angle S_{73}$	$\angle S_{73} - \angle S_{63}$	$\angle S_{63} - \angle S_{53}$	
Ideal $\rightarrow 90^\circ$	$-90^\circ + 9.6^\circ$	$-90^\circ - 10.5^\circ$	$-90^\circ - 6^\circ$	
Port4	S_{54}	S_{64}	S_{74}	S_{84}
IL (dB)	-8.13	-8.44	-7.79	-8.08
Max amp. imb.(dB)	0.65			
PPD	$\angle S_{84} - \angle S_{74}$	$\angle S_{74} - \angle S_{64}$	$\angle S_{64} - \angle S_{54}$	
Ideal $\rightarrow 90^\circ$	$90^\circ + 9.6^\circ$	$90^\circ - 9.8^\circ$	$90^\circ + 6.3^\circ$	

equals 0.75 dB. On the basis of the sensitivity study, such low values in terms of amplitude imbalance might come from the efforts in terms of crossover design.

V. COMPARISON WITH STATE-OF-THE-ART BUTLER MATRICES

Various Butler matrices, with extended beam concept, are compared in Table 7. The matrix presented in this work does not provide the lowest deviation in terms of PPD. However, as outlined in section IV, this PPD deviation only marginally affects the array factor, with little impact on the spatial angle deviation. Meanwhile, Table 7 enables relating the amplitude imbalance with crossover transmission path isolation. Crossover results sometimes come from previous works so that the provided transmission path isolation values are referred to in these anterior studies. A very interesting feature is that the lower magnitude imbalances correspond to the higher crossover isolation, as illustrated with [19] proving, for a conventional SIW matrix, excellent imbalance

TABLE 6. Extended beam BM2 measurements results at 28 GHz.

Port1	S_{51}	S_{61}	S_{71}	S_{81}
IL (dB)	-8.3	-7.79	-8.6	-7.73
Max amp. imb.(dB)	0.88			
PPD	$\angle S_{81} - \angle S_{71}$	$\angle S_{71} - \angle S_{61}$	$\angle S_{61} - \angle S_{51}$	
Ideal $\rightarrow 45^\circ$	$-45^\circ + 12.3^\circ$	$-45^\circ - 10.6^\circ$	$-45^\circ + 15.9^\circ$	
Port2	S_{52}	S_{62}	S_{72}	S_{82}
IL (dB)	-8.4	-8.2	-7.86	-7.66
Max amp. imb.(dB)	0.74			
PPD	$\angle S_{82} - \angle S_{72}$	$\angle S_{72} - \angle S_{62}$	$\angle S_{62} - \angle S_{52}$	
Ideal $\rightarrow 135^\circ$	$135^\circ + 16.9^\circ$	$135^\circ - 11.7^\circ$	$135^\circ + 10.9^\circ$	
Port3	S_{53}	S_{63}	S_{73}	S_{83}
IL (dB)	-8.34	-7.61	-8.56	-8.22
Max amp. imb.(dB)	0.96			
PPD	$\angle S_{83} - \angle S_{73}$	$\angle S_{73} - \angle S_{63}$	$\angle S_{63} - \angle S_{53}$	
Ideal $\rightarrow -135^\circ$	$-135^\circ + 11.4^\circ$	$-135^\circ - 5.9^\circ$	$-135^\circ + 6^\circ$	
Port4	S_{54}	S_{64}	S_{74}	S_{84}
IL (dB)	-8.1	-8.4	-7.92	-7.78
Max amp. imb.(dB)	0.62			
PPD	$\angle S_{84} - \angle S_{74}$	$\angle S_{74} - \angle S_{64}$	$\angle S_{64} - \angle S_{54}$	
Ideal $\rightarrow 45^\circ$	$45^\circ + 8.3^\circ$	$45^\circ - 7.7^\circ$	$45^\circ + 8.6^\circ$	

thanks to infinite isolation for the first crossover that takes advantage of a 2-layered PCB technology, or with [24] based on their former work on an extremely well-isolated dual-band microstrip crossover [41]. This aspect was enabling them to provide 0.9-dB of ripple in their antenna gain by the end. Our Butler matrix, showing a very good SIW-type crossover isolation of 30 dB, enables 1.1-dB of ripple in array factor as it will be pointed out in section IV. Finally, it might be outlined that the magnitude imbalance of [25], although providing a compact beam forming network, might be explained by crossover issues. The authors refer to their previous work concerning wideband DC-40GHz crossover providing good isolation, inferior or equal to 30 dB, at frequencies lower than 3 GHz but with very high sensitivity of isolation level to frequency. The crossover used in [25] uses a similar principle but on a different substrate which does not enable to relate isolation level to imbalance at 2.45 GHz fairly.

VI. ARRAY PATTERN

The aforementioned measured results are exploited in the calculus of the array factor, AF , to evaluate their impact of imbalance. For Butler matrix BM_n , $n = 1$ or 2 , fed at port i , $i = (1, 2, 3, 4)$, the array factor is named AF_{i-BMn} :

$$\text{VI. } AF_{i-BMn} = \left(\sum_{j=5}^8 |S_{ji-BMn}| \cdot e^{j \cdot \gamma_{ji-BMn}} \right) \quad (8)$$

with $\gamma_{ji-BMn} = \angle S_{ji-BMn} + \beta_0 \cdot j \cdot d \cdot \cos(\theta)$

where β_0 is the free space phase constant. For isotropic sources distanced by $d = 0.5 \cdot \lambda_0$, where λ_0 is the freespace wavelength, (8) results in the colored plots of FIGURE 3, exploiting the same color code as in FIGURE 17. The theoretical AF is plotted as well for comparison in black lines.

Concerning the maximum amplitude, beams present almost the same with the biggest discrepancy equal to 0.23 dB between most performing beam 1L and least performing

TABLE 7. Extended beam BM combinations for enhanced spatial agility.

Ref	Concept	Tech.	Nb of beams	Freq (GHz)	Max. IL (dB)	Max. lmb. (dB)	Mean lmb. (dB)	Max. PPD dev. (°)	Mean PPD dev. (°)	Crossover isolation
[18]	4x4 Conventional	SIW	4	60	2.7	2.8	0.96	17	7.5	26
[19]	4x4 Conventional	SIW	4	12.5	0.9	0.4	0.2	5°	5°	1 st : ∞ 2 nd : N/A
[21]	4x4 Reconfig. couplers	μstrip	8	2.4	2.9	2.4	1.5	3	1.5	25 ¹
[22]	8x8 Steerable PSs	μstrip	8 steerable	2.2	3.2	3.7	1.7	N/A*	N/A*	>20 ²
[23] [#]	4x4 Reconfig. PSs	μstrip	17	2.4	~2	~1	~1	~15	~10	N/A
[24]	4x4 Reconfig. couplers	μstrip	8	6	2.5	0.76	0.44	6	4.7	>35 ³
[25]	4x4 Reconfig. PSs	μstrip	8	2.45	4.1	4.4	2.0	7.8	5.0	N/A ⁴
This work	4x4 Reconfig. PSs	SIW	9	28	2.8	1.3	0.75	17	10.6	30

[#] 2 sets of parameters over 4 are provided. * steerable ¹ on the basis of [39] ² on the basis of [40] ³ on the basis of [41] ⁴ on the basis of [42].

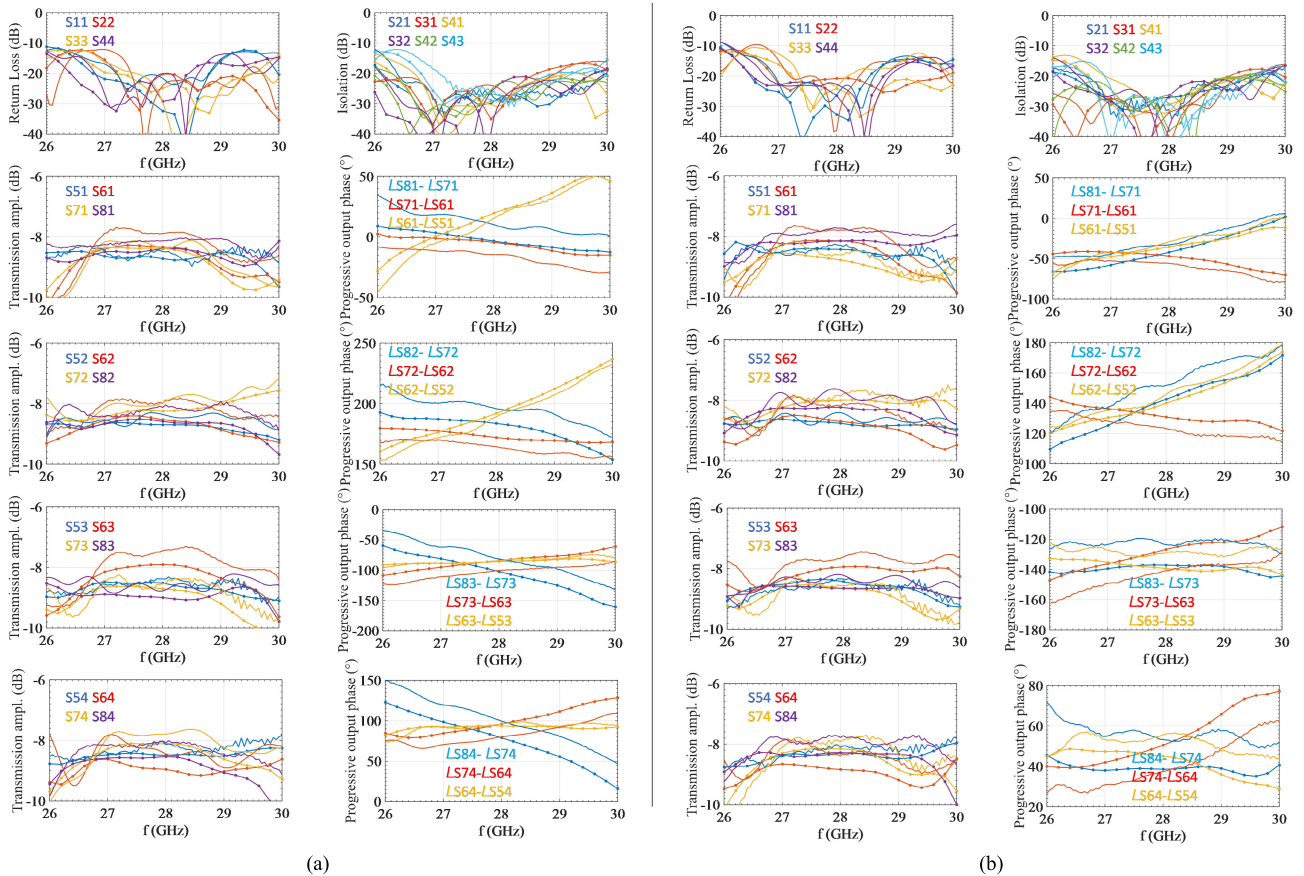


FIGURE 16. a) BM1 and b) BM2 measurements. De-embedded measurements (straight line), simulations (circled lines).

beam 2R (see FIGURE 17 for beam number allocation). The gain of beam 1L is equal to 3.97 dB while the 2R equals 3.74 dB. Overall, the average beam gain is around 3.8 dB, which means a gain loss equal to 2.2 dB compared to the

theoretical 6 dB one. The maximum ripple is 1.1 dB between the beams 2R and 3R, while the minimum is 0.78 dB between 4L and 3L. The typical ripple is 0.8 dB. The calculated beam pointing angles are equal to -89.4° , -50.2° , -30.4° ,

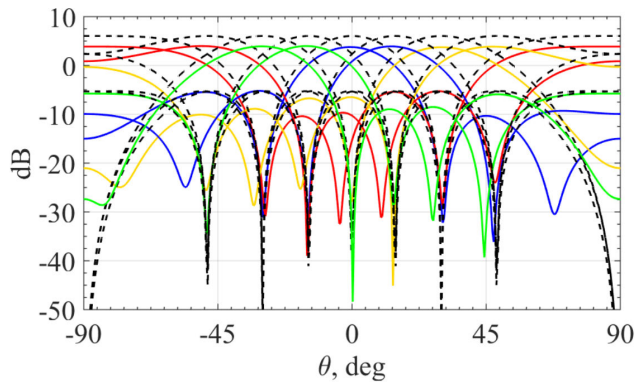


FIGURE 17. Array factor for an extended beam 4×4 BM. Measured BM (colored lines) and theoretical non lossy, with no imbalance, BM (black lines). $d = 0.5 \cdot \lambda_0$.

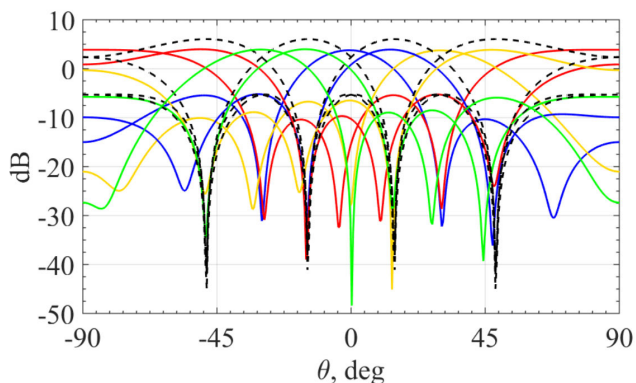


FIGURE 18. Array factor for measured results of an extended beam 4×4 BM (colored lines) and theoretical non lossy, with no imbalance, results of a conventional 4×4 BM (black lines). $d = 0.5 \cdot \lambda_0$.

-15.1° , -0.7° , 13.3° , 30° , 47.1° and 83.1° for the beams from 4L to 4R, respectively. The deviations with respect to the ideal beams pointing are 0.6° , 1.7° , 0.4° , 0.5° , 0.7° , 1.3° , 0° , 1.4° , 6.9° for the beams from 4L to 4R, respectively.

Excepting the observable deviation for beam 4R of almost 7° , most beams keep the same direction within a deviation lower than 2° . In the meantime, the ripple is small, 0.8 dB as a mean value, which guarantees an interesting space coverage between almost half a space. This point is very interesting as it proves that antenna arrays are resilient to output phase imbalance. In counterpart, magnitude imbalance may lead to more important ripple in the AF , and this point has to be avoided as much as possible to provide a wide angular scanning with identical antenna gain. As precised in the sensitivity analysis, particular attention has to be paid towards the crossover transmission path isolation to avoid amplitude imbalance and consequently to limit ripple in AF . The small observable ripple reached herein comes from the particular attention paid to crossover design. Finally, the maximum side-lobe level (SLL) related to the beam 1R, is 2.2 dB, but only for beams 3L and 3R, which is a typical response for those beams in the extended beam concept [23].

Overall, the measured array factor is very similar to the ideal one, except the maximum gain that is 2.2 dB below due to the beamforming network insertion loss (2.13 ± 0.7 dB) as a reminder.

In comparison, the theoretical non-lossy 4×4 conventional BM of FIGURE 18. shows a spatial coverage ranging from -48.6° to $+48.6^\circ$ with a maximum ripple of 3.7 dB.

VII. CONCLUSION

In this study, attention focused on a detailed sensitivity study of a 4×4 Butler matrix. The Monte Carlo analysis was carried out for stand-alone BM devices with the aim to investigate their impact on the overall BM output performance. The crossover transmission path isolation level was pointed out to be an issue for designers. Typically, an isolation of 30 dB should be reached. Analytical electromagnetic equations were provided to strengthen this thesis.

An experimental validation was also described by presenting a BM designed using PCB technology. The proposed BM was based on the extended beam concept and it was implemented through the concept of switched-line SIW phase shifters. The design blocks for a 28-GHz SIW extended beam Butler matrix were introduced and measured. 3-dB coupler and crossover realized in short-slot topology were presented. Afterward, the phase shifters included in the Butler matrix system were discussed. For a proof-of-concept, for each 1-bit phase shifter, two fixed phase shifters were designed, representing either an RF path or the other. They were arranged in the system with the couplers and crossovers, forming two complete Butler matrices. Particular attention was paid to achieve the 30 dB crossover isolation criteria. An IL of 2.13 ± 0.7 dB and a maximum PPD of -15.5° and $+15.7^\circ$ were measured. Based on $0.5 \lambda_0$ evenly spaced isotropic antennas, those results enable a spatial coverage from -89.4° to 83.1° with a maximum array gain of 3.8 dB and a ripple of 1.1 dB for the array factor as compared to the $-48.6^\circ/+48.6^\circ$ spatial coverage, 6-dB of maximum gain, 3.7-dB of ripple of the conventional non-lossy 4×4 Butler matrix array.

ACKNOWLEDGMENT

The authors would like to thank Loïc Vincent, from the CIME-Nanotech for his particular attention paid to measurement tool.

REFERENCES

- [1] M. Ben-Daya, E. Hassini, and Z. Bahroun, "Internet of Things and supply chain management: A literature review," *Int. J. Prod. Res.*, vol. 57, nos. 15–16, pp. 4719–4742, Aug. 2019, doi: [10.1080/00207543.2017.1402140](https://doi.org/10.1080/00207543.2017.1402140).
- [2] T. E. Bogale and L. B. Le, "Massive MIMO and mmWave for 5G wireless HetNet: Potential benefits and challenges," *IEEE Veh. Technol. Mag.*, vol. 11, no. 1, pp. 64–75, Mar. 2016, doi: [10.1109/MVT.2015.2496240](https://doi.org/10.1109/MVT.2015.2496240).
- [3] R. Garg, P. Bhartia, I. J. Bahl, and A. Ittipiboon, *Microstrip Antenna Design Handbook*. Norwood, MA, USA: Artech House, 2001.
- [4] R. J. Mailloux, *Phased Array Antenna Handbook*, 3rd ed. Norwood, MA, USA: Artech House, 2017.

- [5] P. Kasemir, N. Sutton, M. Radway, B. Jeong, T. Brown, and D. S. Filipović, "Wideband analog and digital beamforming," in *Proc. 9th Int. Conf. Telecommun. Mod. Satell., Cable, Broadcast. Services*, Oct. 2009, pp. 372–375, doi: [10.1109/TELSKS.2009.5339545](https://doi.org/10.1109/TELSKS.2009.5339545).
- [6] W. Rotman and R. Turner, "Wide-angle microwave lens for line source applications," *IEEE Trans. Antennas Propag.*, vol. AP-11, no. 6, pp. 623–632, Nov. 1963, doi: [10.1109/TAP.1963.1138114](https://doi.org/10.1109/TAP.1963.1138114).
- [7] J. Blass, "Multidirectional antenna—A new approach to stacked beams," in *Proc. IRE Int. Conv. Rec.*, New York, NY, USA, vol. 8, pp. 48–50, 1960, doi: [10.1109/IRECON.1960.1150892](https://doi.org/10.1109/IRECON.1960.1150892).
- [8] N. J. G. Fonseca, "Printed S-band 4×4 nolen matrix for multiple beam antenna applications," *IEEE Trans. Antennas Propag.*, vol. 57, no. 6, pp. 1673–1678, Jun. 2009, doi: [10.1109/TAP.2009.2019919](https://doi.org/10.1109/TAP.2009.2019919).
- [9] J. Butler. (1961). *Beam-Forming Matrix Simplifies Design of Electronically Scanned Antenna*. Accessed: Nov. 25, 2019. [Online]. Available: <https://ci.nii.ac.jp/naid/10030189740/>
- [10] A. Tajik, A. Shafiei Alavijeh, and M. Fakharzadeh, "Asymmetrical 4×4 Butler matrix and its application for single layer 8×8 Butler matrix," *IEEE Trans. Antennas Propag.*, vol. 67, no. 8, pp. 5372–5379, Aug. 2019, doi: [10.1109/TAP.2019.2916695](https://doi.org/10.1109/TAP.2019.2916695).
- [11] Y.-L. Li, Q. S. Liu, S. Sun, and S. S. Gao, "A miniaturised Butler matrix based on patch hybrid couplers with cross slots," in *Proc. IEEE Antennas Propag. Soc. Int. Symp. (APSURSI)*, Orlando, FL, USA, Jul. 2013, pp. 2145–2146, doi: [10.1109/APS.2013.6711731](https://doi.org/10.1109/APS.2013.6711731).
- [12] G. Tian, J.-P. Yang, and W. Wu, "A novel compact Butler matrix without phase shifter," *IEEE Microw. Wireless Compon. Lett.*, vol. 24, no. 5, pp. 306–308, May 2014, doi: [10.1109/LMWC.2014.2306898](https://doi.org/10.1109/LMWC.2014.2306898).
- [13] S. Gruszczynski and K. Winca, "Broadband 4×4 Butler matrices as a connection of symmetrical multisection coupled-line 3-dB directional couplers and phase correction networks," *IEEE Trans. Microw. Theory Techn.*, vol. 57, no. 1, pp. 1–9, Jan. 2009, doi: [10.1109/TMTT.2008.2009081](https://doi.org/10.1109/TMTT.2008.2009081).
- [14] T.-H. Lin, S.-K. Hsu, and T.-L. Wu, "Bandwidth enhancement of 4×4 Butler matrix using broadband forward-wave directional coupler and phase difference compensation," *IEEE Trans. Microw. Theory Techn.*, vol. 61, no. 12, pp. 4099–4109, Dec. 2013, doi: [10.1109/TMTT.2013.2288597](https://doi.org/10.1109/TMTT.2013.2288597).
- [15] F. Wu and L. Sun, "Miniaturization of 4×4 Butler matrix using high slow-wave factor structure," in *Proc. IEEE 2nd Adv. Inf. Technol., Electron. Automat. Control Conf. (IAEAC)*, Sep. 2017, pp. 1–4.
- [16] K. Ding, F. He, X. Ying, and J. Guan, "A compact 8×8 Butler matrix based on double-layer structure," in *Proc. 5th IEEE Int. Symp. Microw., Antenna, Propag. EMC Technol. Wireless Commun.*, Oct. 2013, pp. 650–653, doi: [10.1109/MAPE.2013.6689925](https://doi.org/10.1109/MAPE.2013.6689925).
- [17] S. Yamamoto, J. Hirokawa, and M. Ando, "A beam switching slot array with a 4-way Butler matrix installed in a single layer post-wall waveguide," in *Proc. IEEE Antennas Propag. Soc. Int. Symp.*, San Antonio, TX, USA, vol. 1, Jun. 2002, pp. 138–141, doi: [10.1109/APS.2002.1016269](https://doi.org/10.1109/APS.2002.1016269).
- [18] C.-J. Chen and T.-H. Chu, "Design of a 60-GHz substrate integrated waveguide Butler matrix—A systematic approach," *IEEE Trans. Microw. Theory Techn.*, vol. 58, no. 7, pp. 1724–1733, Jul. 2010, doi: [10.1109/TMTT.2010.2050097](https://doi.org/10.1109/TMTT.2010.2050097).
- [19] A. A. M. Ali, N. J. G. Fonseca, F. Coccetti, and H. Aubert, "Design and implementation of two-layer compact wideband Butler matrices in SIW technology for Ku-band applications," *IEEE Trans. Antennas Propag.*, vol. 59, no. 2, pp. 503–512, Feb. 2011, doi: [10.1109/TAP.2010.2093499](https://doi.org/10.1109/TAP.2010.2093499).
- [20] D. E. Hocevar, M. R. Lightner, and T. N. Trick, "A study of variance reduction techniques for estimating circuit yields," *IEEE Trans. Comput.-Aided Design Integr.*, vol. CAD-2, no. 3, pp. 180–192, Jul. 1983, doi: [10.1109/TCAD.1983.1270035](https://doi.org/10.1109/TCAD.1983.1270035).
- [21] K. Ding and A. A. Kishk, "Extension of Butler matrix number of beams based on reconfigurable couplers," *IEEE Trans. Antennas Propag.*, vol. 67, no. 6, pp. 3789–3796, Jun. 2019, doi: [10.1109/TAP.2019.2902668](https://doi.org/10.1109/TAP.2019.2902668).
- [22] C.-C. Chang, R.-H. Lee, and T.-Y. Shih, "Design of a beam switching/steering Butler matrix for phased array system," *IEEE Trans. Antennas Propag.*, vol. 58, no. 2, pp. 367–374, Feb. 2010, doi: [10.1109/TAP.2009.2037693](https://doi.org/10.1109/TAP.2009.2037693).
- [23] H. N. Chu and T.-G. Ma, "An extended 4×4 Butler matrix with enhanced beam controllability and widened spatial coverage," *IEEE Trans. Microw. Theory Techn.*, vol. 66, no. 3, pp. 1301–1311, Mar. 2018, doi: [10.1109/TMTT.2017.2772815](https://doi.org/10.1109/TMTT.2017.2772815).
- [24] H. Ren, B. Arigong, M. Zhou, J. Ding, and H. Zhang, "A novel design of 4×4 Butler matrix with relatively flexible phase differences," *IEEE Antennas Wireless Propag. Lett.*, vol. 15, pp. 1277–1280, 2016, doi: [10.1109/LAWP.2015.2504719](https://doi.org/10.1109/LAWP.2015.2504719).
- [25] A. Tajik, A. Shafiei Alavijeh, and M. Fakharzadeh, "Asymmetrical 4×4 Butler matrix and its application for single layer 8×8 Butler matrix," *IEEE Trans. Antennas Propag.*, vol. 67, no. 8, pp. 5372–5379, Aug. 2019, doi: [10.1109/TAP.2019.2916695](https://doi.org/10.1109/TAP.2019.2916695).
- [26] H. J. Riblet, "The short-slot hybrid junction," *Proc. IRE*, vol. 40, no. 2, pp. 180–184, Feb. 1952, doi: [10.1109/JRPROC.1952.274021](https://doi.org/10.1109/JRPROC.1952.274021).
- [27] G. F. Engen and C. A. Hoer, "Thru-reflect-line: An improved technique for calibrating the dual six-port automatic network analyzer," *IEEE Trans. Microw. Theory Techn.*, vol. MTT-27, no. 12, pp. 987–993, Dec. 1979, doi: [10.1109/TMTT.1979.1129778](https://doi.org/10.1109/TMTT.1979.1129778).
- [28] T. Yang, M. Ettore, and R. Sauleau, "Novel phase shifter design based on substrate-integrated-waveguide technology," *IEEE Microw. Wireless Compon. Lett.*, vol. 22, no. 10, pp. 518–520, Oct. 2012, doi: [10.1109/LMWC.2012.2217122](https://doi.org/10.1109/LMWC.2012.2217122).
- [29] K. Sellal, L. Talbi, and T. A. Denidni, "A 28 GHz phase shifter using substrate integrated waveguide," in *Proc. 12th Int. Symp. Antenna Technol. Appl. Electromagn. Can. Radio Sci. Conf.*, 2006, pp. 1–4.
- [30] L. Wu, A. J. Farrall, and P. R. Young, "Substrate integrated waveguide switched beam antenna," *IEEE Trans. Antennas Propag.*, vol. 63, no. 5, pp. 2301–2305, May 2015, doi: [10.1109/TAP.2015.2405085](https://doi.org/10.1109/TAP.2015.2405085).
- [31] B. Khalichi, S. Nikmehr, and A. Pourziad, "Reconfigurable SIW antenna based on RF-MEMS switches," *Prog. Electromagn. Res.*, vol. 142, pp. 189–205, 2013, doi: [10.2528/PIER13070204](https://doi.org/10.2528/PIER13070204).
- [32] J. Hu, Z.-C. Hao, and Z.-W. Miao, "A circular polarization reconfigurable substrate integrated waveguide antenna," in *Proc. IEEE Int. Conf. Ubiquitous Wireless Broadband (ICUWB)*, Nanjing, China, Oct. 2016, pp. 1–3, doi: [10.1109/ICUWB.2016.7790534](https://doi.org/10.1109/ICUWB.2016.7790534).
- [33] Y. Geng, J. Wang, Y. Li, Z. Li, M. Chen, and Z. Zhang, "Radiation pattern-reconfigurable leaky-wave antenna for fixed-frequency beam steering based on substrate-integrated waveguide," *IEEE Antennas Wireless Propag. Lett.*, vol. 18, no. 2, pp. 387–391, Feb. 2019, doi: [10.1109/LAWP.2019.2892057](https://doi.org/10.1109/LAWP.2019.2892057).
- [34] V. Sekar, M. Armendariz, and K. Entesari, "A 1.2–1.6-GHz substrate-integrated-waveguide RF MEMS tunable filter," *IEEE Trans. Microw. Theory Techn.*, vol. 59, no. 4, pp. 866–876, Apr. 2011, doi: [10.1109/TMTT.2011.2109006](https://doi.org/10.1109/TMTT.2011.2109006).
- [35] R. F. Xu, B. S. Izquierdo, and P. R. Young, "Switchable substrate integrated waveguide," *IEEE Microw. Wireless Compon. Lett.*, vol. 21, no. 4, pp. 194–196, Apr. 2011, doi: [10.1109/LMWC.2011.2108274](https://doi.org/10.1109/LMWC.2011.2108274).
- [36] A. B. Numan, J. F. Frigon, and J. J. Laurin, "Single-pole single-throw switch for substrate-integrated waveguide," *IEEE Microw. Wireless Compon. Lett.*, vol. 28, no. 3, pp. 221–223, Mar. 2018, doi: [10.1109/LMWC.2018.2804259](https://doi.org/10.1109/LMWC.2018.2804259).
- [37] I. Lim and S. Lim, "Substrate-integrated-waveguide (SIW) single-pole-double-throw (SPDT) switch for X-band applications," *IEEE Microw. Wireless Compon. Lett.*, vol. 24, no. 8, pp. 536–538, Aug. 2014, doi: [10.1109/LMWC.2014.2321065](https://doi.org/10.1109/LMWC.2014.2321065).
- [38] Y. J. Cheng, K. Wu, and W. Hong, "Substrate integrated waveguide (SIW) broadband compensating phase shifter," in *IEEE MTT-S Int. Microw. Symp. Dig.*, Jun. 2009, pp. 845–848, doi: [10.1109/MWSYM.2009.5165829](https://doi.org/10.1109/MWSYM.2009.5165829).
- [39] W. Liu, Z. Zhang, Z. Feng, and M. Iskander, "A compact wideband microstrip crossover," *IEEE Microw. Wireless Compon. Lett.*, vol. 22, no. 5, pp. 254–256, May 2012, doi: [10.1109/LMWC.2012.2190270](https://doi.org/10.1109/LMWC.2012.2190270).
- [40] M. Bona, L. Manholm, J. P. Starski, and B. Svensson, "Low-loss compact Butler matrix for a microstrip antenna," *IEEE Trans. Microw. Theory Techn.*, vol. 50, no. 9, pp. 2069–2075, Sep. 2002, doi: [10.1109/TMTT.2002.802318](https://doi.org/10.1109/TMTT.2002.802318).
- [41] J. Shao, H. Ren, B. Arigong, C. Li, and H. Zhang, "A fully symmetrical crossover and its dual-frequency application," *IEEE Trans. Microw. Theory Techn.*, vol. 60, no. 8, pp. 2410–2416, Aug. 2012, doi: [10.1109/TMTT.2012.2198229](https://doi.org/10.1109/TMTT.2012.2198229).
- [42] A. Tajik, M. Fakharzadeh, and K. Mehrany, "DC to 40-GHz compact single-layer crossover," *IEEE Microw. Wireless Compon. Lett.*, vol. 28, no. 8, pp. 642–644, Aug. 2018, doi: [10.1109/LMWC.2018.2843134](https://doi.org/10.1109/LMWC.2018.2843134).



GIUSEPPE ACRI received the B.S. degree in electronics engineering and the M.S. degree in telecommunications engineering from the University of Calabria, Italy, in 2012 and 2016, respectively, and the Ph.D. degree from the RFIC-Laboratory, University of Grenoble Alpes, in 2020. From 2015 to 2016, he did an Internship at the IMEP-LaHC, Grenoble, France, during which he designed slow-wave passive devices in advanced CMOS technology for mm-wave applications. He was involved in design and implementation of passive RF and millimeter-wave components and switched beam array antennas networks with the University of Grenoble Alpes. From 2020 to 2021, his research interest was in design and implementation of passive devices in BCB 3D-packaging technology for sub-THz applications. He worked at Asygn, Grenoble, as RF/mm-Wave Designer. He is currently working at NXP, Toulouse, and a RF/mm-Wave Designer. The focus of his work is on RF Built-In Self Test (BIST) circuitry design in CMOS28nm, for automotive applications.



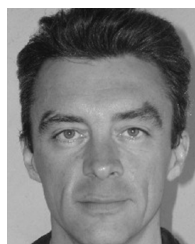
JORDAN CORSI received the master's degree in wireless integrated circuits and systems (WICS) from Université Grenoble Alpes (UGA), Grenoble, France, in 2018, where he is currently pursuing the Ph.D. degree in optics and radio frequency with the RFIC-Laboratory. His current research interests include the development of passive devices in RF and millimeter-waves frequency band using a novel topology of substrate integrated waveguide.



FLORENCE PODEVIN (Member, IEEE) received the Engineering degree in electronics and microelectronics from the École centrale de Lille, Villeneuve-d'Ascq, France, in 1998, and the M.Sc. degree in electronics and microelectronics and the Ph.D. degree in microelectronics from the Université des Sciences et Technologies de Lille (USTL), Villeneuve-d'Ascq, in 1998 and 2001, respectively. In 2001, she joined the Institute of Microelectronics, Electromagnetism and Photonics (IMEP, IMEP-LAHC), Grenoble, France, as an Assistant Professor. She is currently an Associate Professor with the Laboratory of Radio Frequency Integrated Circuits, University of Grenoble Alpes, Grenoble. Her research interests include tunable and miniaturized devices, such as phase shifters, power dividers, couplers, or codesign between passive and active devices with some large interest on distributed amplifiers. She is also involved in RFIC design. She benefits from a great experience in terms of slow-wave transmission lines, at millimeter-wave frequencies, and in CMOS and BiCMOS technologies or on advanced substrates dedicated to millimeter waves. She has authored or coauthored more than 110 papers published in international journals and national or international conferences and the co-holder of three patents.



EMMANUEL PISTONO received the Ph.D. degree from the Grenoble INP, Grenoble, France, in 2006. In 2007, he joined Université Joseph Fourier, Grenoble (University Grenoble Alpes) and the IMEP-LAHC Laboratory, as an Assistant Professor. Since 2018, he has been a member of the RFIC-Laboratory, Université Grenoble Alpes, where he is also an Associate Professor. His research interests include miniaturized and high-performance RF/millimeter-wave passive circuits in different technologies, such as PCB, CMOS, and alternative technologies.



PHILIPPE FERRARI (Senior Member, IEEE) received the Ph.D. degree (Hons.) from the Institut National Polytechnique de Grenoble (INPG), France, in 1992. Since 2004, he has been a Professor at the University Grenoble Alpes, Grenoble, France. His research interests include tunable and miniaturized devices, such as filters, phase shifters, matching networks, couplers, power dividers, and VCOs. These devices are developed in many technologies, PCB, CMOS/BiCMOS, and nanowires, at RF and mm-wave frequencies. He has worked towards the development of slow wave CPW, and developed new topologies of slow-wave transmission lines, based on microstrip lines and SIWs, respectively. He is the author or coauthor of more than 250 papers published in international journals or conferences, and the co-holder of six patents. He is a member of the Editorial Board of the *International Journal on RF and Microwave Computer-Aided Engineering* (Wiley), an Associate Editor of the *International Journal of Microwave and Wireless Technologies* (EuMA), and a member of the Editorial Board of *Electronics Letters*.



LUIGI BOCCIA (Senior Member, IEEE) was born in Lungro, Italy, in 1975. He received the degree in information technology engineering from the University of Calabria, Rende, Italy, in 2000, and the Ph.D. degree in electronics engineering from the University Mediterranea of Reggio Calabria, Reggio Calabria, Italy, in 2003. From 2005 to 2021, he was an Assistant Professor in electromagnetics at the University of Calabria, where he is currently an Associate Professor. His current research interests include active antennas, reflectarrays, beam-scanning antennas, and micro- and millimeter-wave IC design. He is also a member of the European Microwave Association (EuMA) and the Società Italiana di Elettromagnetismo (SIEm). He serves as an Associate Editor for the IEEE MICROWAVE AND WIRELESS COMPONENTS LETTERS and the *International Journal of Microwave and Wireless Technologies* (Cambridge University Press). He is the Co-Editor of the *Space Antenna Handbook* (Wiley, 2012).

...

Open Access funding provided by 'Università della Calabria' within the CRUI CARE Agreement